Progress In Electromagnetics Research, Vol. 119, 155–170, 2011

AN IMPROVED POLAR FORMAT ALGORITHM WITH PERFORMANCE ANALYSIS FOR GEOSYNCHRONOUS CIRCULAR SAR 2D IMAGING

Q. Liu [1, 2, 3, *], W. Hong [1, 2], W.-X. Tan [1, 2], Y. Lin [1, 2], Y.-P. Wang [1, 2], and Y.-R. Wu [1, 2]

[1]National Key Laboratory of Science and Technology on Microwave Imaging, No. 19, BeiSiHuan XiLu, Beijing, China

[2]Institute of Electronics, Chinese Academy of Sciences, No. 19, BeiSiHuan XiLu, Beijing, China

[3]Graduate University of Chinese Academy of Sciences, No. 19A, YuQuanLu, Beijing, China

Abstract—This paper presents an improved polar format algorithm (PFA) for geosynchronous synthetic aperture radar which undergoes a near-circular track (GeoCSAR). GeoCSAR imaging geometry and signal formulation considering orbit perturbations were derived to ensure accurate slant range between antenna and targets. The illuminated area is more than one million square kilometers due to the long slant distance, resulting in large amount of data to be processed and that the scene is a spherical crown rather than a plane. By assuming spherical wavefronts instead of planar wavefronts, improved polar format algorithm (PFA) was proposed to focus GeoCSAR raw data on a spherical reference surface (ground surface), so that the size of focused scene is no longer limited by the range curvature phase error. Thus, this method could deal with large area imaging for GeoCSAR precisely and efficiently. The implementation procedure, computational complexity, phase error and achievable resolution were presented to show the focusing capabilities of this imaging algorithm. Numerical simulation was further performed to validate the feasibility of this imaging algorithm and the correctness of analysis.

Received 5 June 2011, Accepted 14 July 2011, Scheduled 25 July 2011

* Corresponding author: Qi Liu (cadyfire@163.com).

1. INTRODUCTION

Geosynchronous Synthetic Aperture Radar (GeoSAR) has received more and more attention since it possesses many advantages compared to the low-earth orbit SAR [1]. For example, daily images of earth can be acquired which benefit from the short revisit cycle of GeoSAR (24 hours); benefit from the long slant range, the footprint size of antenna-beam can be very large. The daily track of GeoSAR could be "Figure 8"-like, near-circular or near-ellipse. Conventional GeoSAR usually undergoes "Figure 8" track and corresponding imaging algorithms were only based on the linear aperture [2, 3], and the whole track were not fully utilized. In this paper, GeoSAR which undergoes a near-circular track is considered and called as Geosynchronous Circular SAR (GeoCSAR) to distinguish it from the conventional GeoSAR.

GeoCSAR imaging is faced with several problems: 1) The orbit is usually influenced by perturbations, such as anisotropic geopotential, luni-solar attraction and solar radiation pressure [4]. The orbit perturbations result in variation of geosynchronous orbit elements, and disturb the regular motion of GeoCSAR; 2) The synthetic aperture of GeoCSAR is a near-ellipse circle being divided into several sub-apertures for 2D imaging, which means sub-apertures are irregular and could not be approximated by lines or standard circular arcs; 3) The observation area is very large and echoed data are of large volume.

For the first problem, it can be solved by taking into account of the effect of orbit perturbation when establishing imaging model to ensure accurate slant range between antenna and targets. For the second and third problems, although those time domain imaging algorithms, such as Back-Projection (BP) algorithm, could be used for the case of arbitrary aperture, these algorithms are particularly time-consuming for large area imaging [5–7]. The existing frequency-domain imaging methods based on wavefront reconstruction theory for sub-aperture or all-aperture Circular SAR is efficient, however, they could only be applied to ideal circular geometries [5–8].

Polar Format Algorithm (PFA) operates in the azimuth-time, range-frequency domain [9–12], and has the potential to adapt to non-ideal tracks [10, 11]. However, traditional PFA assumes planar wavefronts around a central reference point in the imaged scene, resulting in the presence of range curvature phase error which limits the size of focused scene [9, 12, 13]. It can not be applied to GeoCSAR directly without modification, since the imaging area of GeoCSAR is much larger than traditional low-earth orbit SAR and airborne SAR. In this paper, imaging model is established with orbit perturbation.

Then, by assuming spherical wavefronts instead of planar wavefronts (which is close in its spirit to the method in [14]), GeoCSAR raw data are focused on a spherical reference surface (ground surface), so the size of focused scene is no longer limited by the range curvature phase error.

The remainder of the paper is organized as follows: GeoCSAR sub-aperture imaging geometry and imaging model are described in Section 2. The improved PFA algorithm for GeoCSAR 2D imaging is presented in Section 3. Reconstruction procedure, computational complexity, phase errors and image resolution are also given. Numerical simulation is shown in Section 4 and Section 5 concludes this paper.

2. GEOCSAR IMAGING GEOMETRY AND MODEL

In the MEGSD (Mean Equatorial Geocentric System of Date) reference frame, the orbit of satellite is described by orbit element set $\mathbb{S} = \{a, e, i, \Omega, \omega, \nu\}^{\mathrm{T}}$, where the six elements in $\mathbb{S}$ denote semi-major axis, eccentricity, inclination, right ascension of the ascending node, argument of perigee and true anomaly, respectively. In order to facilitate analysis, define the unperturbed orbit element set as $\mathbb{S}_0 = \{a_0, e_0, i_0, \Omega_0, \omega_0, \nu_0\}^{\mathrm{T}}$, where $a_0 = 42164.2\,\mathrm{km}$, ν_0 is a function of azimuth slow time t_m that satisfies Kepler's differential equation [4],

$$d\nu_0/dt_m = \sqrt{\mu/a_0^3(1-e_0^2)^3}(1+e_0\cos\nu_0)^2 \tag{1}$$

The distance between satellite to earth center r_P is a function of ν,

$$r_P = a(1-e^2)/(1+e\cos\nu) \tag{2}$$

The latitude φ and longitude λ can be expressed by $\mathbb{S}$

$$\begin{cases} \lambda = \Omega - G_0 + \arg[\cos(\omega+\nu) + j\sin(\omega+\nu)\cos i] - \psi t_m \\ \phi = \arcsin(\sin(\omega+\nu)\sin i) \end{cases} \tag{3}$$

where G_0 denotes Greenwith sidereal angle. Since it is not possible to express ν explicitly in closed analytical form as a function of t_m, (3) is approximated by power series expansion to degree one with the assumption of $e^2 \approx 0$, $\sin i \approx i$ as

$$\lambda \approx \lambda_0 + 2e\sin\nu, \quad \phi \approx i\sin(\omega+\nu) \tag{4}$$

where $\lambda_0 = \Omega - G_0 + \arg[\cos(\omega+\nu) + j\sin(\omega+\nu)\cos i]$. In (4), it shows two important motion components: 1) harmonic motion in longitude, due to orbit's eccentricity e; 2) harmonic motion in latitude, due to satellite orbit's inclination i. When $\omega = \pi/2$ or $3\pi/2$, $i = 2e$, it yields $(\lambda-\lambda_0)^2+\varphi^2 \approx i^2$ and the subsatellite ground track is approximately a

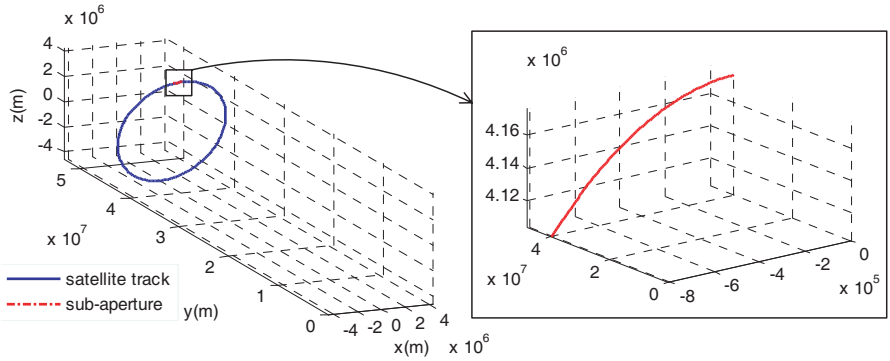

Figure 1. Simulated satellite track.

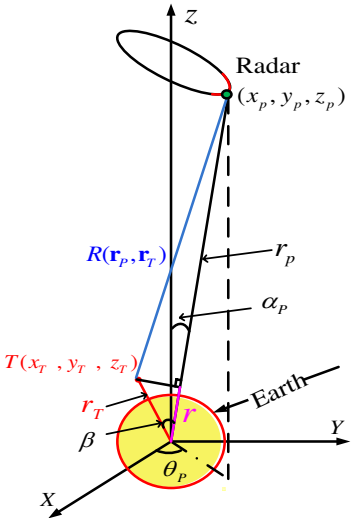

Figure 2. GeoCSAR imaging geometry.

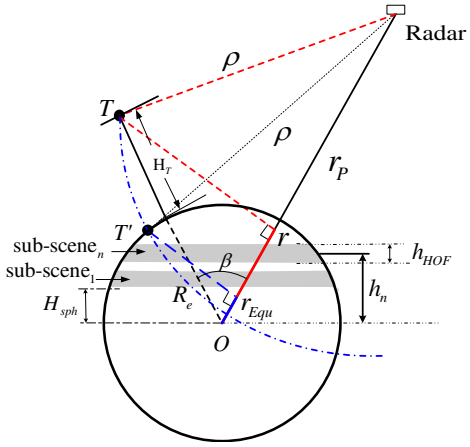

Figure 3. Sketch map of range resampling.

circle. Figure 1 shows the satellite track simulated by direct numerical integration of (2), where main short-period orbit perturbations (e.g., zonal and tesseral terms of earth's gravity and luni-solar perturbations) are considered [4].

Figure 2 shows GeoCSAR imaging geometry in earth-rotating coordinate system. For the sake of clarity, assume $\Omega = 0$. The Y-Z plane is equatorial plane of earth. Y axis points toward east and X axis toward north. Satellite position vector is denoted by $\mathbf{r}_P = (r_P, \alpha_P, \theta_P)$

in spherical coordinates, where α_P and θ_P can be calculated according to (4)

$$\begin{cases} \alpha_P = \arg\left(\sqrt{\sin^2\phi + \cos^2\phi\cos^2\lambda} + \cos\phi\sin\lambda\right) \approx i \\ \theta_P = \arg(\cos\phi + j\cos\phi\cos\lambda) \approx -\nu \end{cases} \tag{5}$$

Let $\mathbf{r}_T$ be position vector of a given target T which is located near earth surface. $\mathbf{r}_P(t_m)$ and $\mathbb{S}(t_m)$ in disturbed orbit are given by

$$\mathbf{r}_P(t_m) = \mathbf{r}_{P_0}(t_m) + \Delta\mathbf{r}_P(t_m), \quad \mathbb{S}(t_m) = \mathbb{S}_0(t_m) + \Delta\mathbb{S}(t_m) \tag{6}$$

where $\mathbf{r}_{P_0}(t_m)$ is derived from unperturbed orbit elements $\mathbb{S}_0$ using (2) and (5). $\Delta\mathbf{r}_P(t_m)$ and $\Delta\mathbb{S}(t_m)$ denote the offsets caused by orbit perturbations. Since $\Delta\mathbb{S}(t_m) \ll \mathbb{S}(t_m)$, (6) can be approximated as [4]

$$\mathbf{r}_P(t_m) = \mathbf{r}_{P_0}(t_m) + \Delta\mathbf{r}_P(t_m), \quad \Delta\mathbf{r}_P(t_m) = \left.\frac{\partial\mathbf{r}_P}{\partial\mathbb{S}}\right|_{\mathbb{S}_0(t_m)} \Delta\mathbb{S}(t_m) \tag{7}$$

$\Delta\mathbb{S}(t_m)$ can be obtained by orbital perturbation models and orbit measurement data. Substituting $\Delta\mathbb{S}(t_m)$ into (7), the satellite position is

$$\mathbf{r}_P(t_m) = \mathbf{r}_{P_0}(t_m) + \begin{bmatrix} m_{11} & m_{12} & 0 & 0 & 0 & m_{16} \\ 0 & 0 & 1 & 0 & 0 & 0 \\ 0 & 0 & 0 & 0 & 0 & -1 \end{bmatrix} \cdot \Delta\mathbb{S}(t_m) \tag{8}$$

where $m_{11} = \frac{1-e_0^2}{1+e_0\cos\nu_0(t_m)}$, $m_{12} = -\frac{2a_0e_0}{1+e_0\cos\nu_0(t_m)} - \frac{a_0(1-e_0^2)\cos\nu_0(t_m)}{(1+e_0\cos\nu_0(t_m))^2}$,

$$m_{16} = \frac{a_0(1-e_0^2)e_0\sin\nu_0(t_m)}{(1+e_0\cos\nu_0(t_m))^2}$$

As shown in Figure 3, the instantaneous slant range $R(\mathbf{r}_P, \mathbf{r}_T) = \sqrt{r_P^2 + r_T^2 - 2r_Pr_T\cos\beta}$, where β is the angle between position vector $\mathbf{r}_P(t_m)$ and $\mathbf{r}_T$,

$$\cos\beta = \sin\alpha_P\sin\alpha_T\cos(\theta_p - \theta_T) + \cos\alpha_P\cos\alpha_T \tag{9}$$

Then, echoed signal from target T after range compression is

$$E(k_r, \mathbf{r}_P) = I(r_T, \alpha_T, \theta_T)\exp\{-jk_rR(\mathbf{r}_P, \mathbf{r}_T)\} \tag{10}$$

where $I(r_T, \alpha_T, \theta_T)$ is the complex reflectivity of targets. k_r is two-way frequency wavenumber, and is related to instantaneous frequency f_r and speed of light c via $k_r = 4\pi(f_c+f_r)/c$. f_c is the carrier frequency. $k_r \in [k_{r\min}, k_{r\max}]$, where $k_{r\min}$ and $k_{r\max}$ denote wavenumbers at the minimum and maximum frequencies, respectively.

3. IMPROVED PFA FOR GEOCSAR 2D IMAGING

In this section, improved PFA for large area imaging of GeoCSAR is addressed firstly. Then, reconstruction procedure and corresponding computational complexity are given. Finally, phase error and image resolution are discussed.

3.1. Improved PFA

Let H_T be height of target T. Denote $\rho = c{\cdot}t/2$ as range spatial domain. Figure 3 shows the sketch map of range resampling, $r_T = R_e + H_T$,

$$r = r_T \cos\beta = \frac{r_P^2 + r_T^2 - \rho^2}{2r_P} \tag{11}$$

Assume that all the targets are located exactly on the reference surface, i.e., $H_T = 0$. Then, ρ is mapped to r_{Equ} instead of r, as shown in Figure 3, and

$$r_{Equ} = \frac{r_P^2 + R_e^2 - \rho^2}{2r_P} \tag{12}$$

Projecting ρ to r can be realized by 1D resampling in spatial domain, then the resulting signal is

$$S_r(r, \mathbf{r}_P) = S_r(\rho, \mathbf{r}_P) \cdot \exp\{j(k_{rc}\rho - k_c' r)\} = q_r(r - r_{Equ}) \cdot \exp\{-jk_c' \cdot r_{Equ}\} \tag{13}$$

where $S_r(\rho, \mathbf{r}_P) = \int E(k_r, \mathbf{r}_P) \exp\{j(k_r - k_{rc})\rho\}$ and

$$\begin{gathered} r_{Equ} = \frac{r_P^2 + R_e^2 - R^2(\mathbf{r}_P, \mathbf{r}_T)}{2r_P} \quad k_c' = k_{rc}\left(\frac{d\rho}{dr}\bigg|_{\rho=\rho_{\text{mid}}}\right) = -k_{rc}\frac{r_P}{\rho_{\text{mid}}} \\ B' \approx B_r\left|\frac{d\rho}{dr}\bigg|_{\rho=\rho_{\text{mid}}}\right| = \frac{r_P}{\rho_{\text{mid}}}B_r \quad q_r(r - r_{Equ}) \approx \text{sinc}\left(\frac{2B'}{c}(r - r_{Equ})\right) \end{gathered} \tag{14}$$

After resampling, the bandwidth B' and wavenumber k_c' are a function of r_P, thus they will vary with the satellite position. In the resampling process, k_c' needs to be set at a fixed value of $-(r_P/\rho_0)_{\text{mid}} \cdot k_{rc}$.

As for image formation, signal phase places a dominant role, so the approximation made in the amplitude function $q_r \approx \text{sinc}(2B'(r - r_{Equ})/c)$ and the reflectivity of target $I(x_T, y_T, z_T)$ does not affect image quality. We assume $I(x_T, y_T, z_T) = 1$ and discuss the phase of the signal separately in the following. Via range FFT,

$$S_r(k', \mathbf{r}_P) = \int S_r(r, \mathbf{r}_P) \cdot \exp\left\{-j(k' - k_c')r\right\} dr = \exp\left\{-jk' \cdot r_{Equ}\right\} \tag{15}$$

Substituting $R(\mathbf{r}_P, \mathbf{r}_T)$, (9) and (14) into (15), then

$$S_r\left(k', \mathbf{r}_P\right) = \exp\{-j(k_P \cos\theta_P)x_T - j(k_P \sin\theta_P)y_T - jk_P \cot\alpha_P(z_T)\} \tag{16}$$

where $k_P = k' \sin\alpha_P$. The angle α_P varies along with the motion of satellite (see (8)). Figure 4 shows data surface in frequency domain which takes point target locating at $(44°46'28'', \text{N } 0°\text{E})$ with $H_T = 0$ for example. Let $k_x = k_P \cdot \cos\theta_P$, $k_y = k_P \cdot \sin\theta_P$, $k_z = k_P \cdot \cot\alpha_P$, the

received data in the spatial frequency domain is a non-planar ribbon due to the non-planar collection.

As shown in Figure 3, choose a plane that is perpendicular to Z axis and h_n away from X-Y plane as the focus plane; that is, multiplying (16) with a reference function,

$$H(k_P, h_n) = k_P \cdot \cot \alpha_P \cdot h_n \tag{17}$$

Then the signal in (16) becomes

$$S_Z(k', \mathbf{r}_P) = \exp\{-j(k_P \cos\theta_P)x_T - j(k_P \sin\theta_P)y_T - jk_P \cot\alpha_P(z_T - h_n)\} \tag{18}$$

Then, via interpolation, the polar samples of $S_Z(k', \mathbf{r}_P)$ are converted to 2D frequency format:

$$S_Z(k_x, k_y) = \exp\left\{-jk_x x_T - jk_y y_T - j\sqrt{k_x^2 + k_y^2}\cot\alpha_P(z_T - h_n)\right\} \tag{19}$$

The 2D inverse Fourier transform of $S_Z(k_x, k_y)$ is the desired 2D image. From third term on the right of (19), if height of scatterer z_T equals to that of focus plane h_n, scatterers could be well focused. However, because of the spherical character of imaging area, scatterers are usually outside the focus plane. Within a certain target altitude h_{HOF} (depending on the amount and nature of the out-of-plane motion), scatterers outside the focus plane could also be well focused. In the following , the value of h_{HOF} is derived.

Let θ_c be center of θ_P in a certain sub-aperture, as shown in Figure 5, $\theta' = \theta_P - \theta_c$, then

$$R(\mathbf{r}_P, \mathbf{r}_T) = u_T \cos\theta' + v_T \sin\theta' + h_Z \cot\alpha_P \tag{20}$$

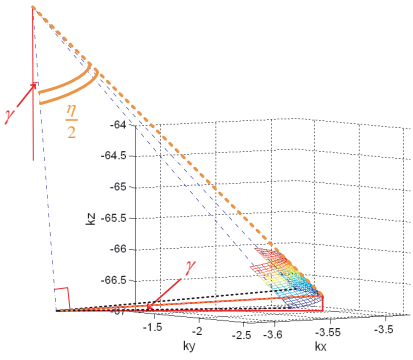

Figure 4. Data surface in frequency domain.

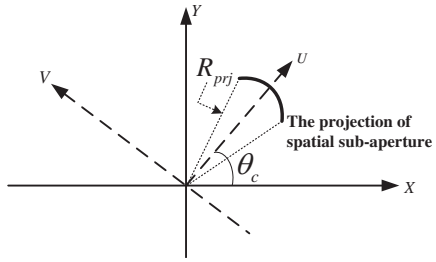

Figure 5. Projection of spatial sub-aperture.

where $u_T = x_T \cos\theta_c + y_T \sin\theta_c$, $v_T = -x_T \sin\theta_c + y_T \cos\theta_c$. The projection of satellite track on ground is a circle and R_{prj} is constant, thus $\sin\alpha_P = R_{prj}/r_P$. Utilizing $\nu \approx \theta_P$, (2) can be expressed as

$$r_p \approx \frac{a(1-e^2)}{1+e\cos\theta_P} = \frac{a(1-e^2)}{1+e\cos(\theta'+\theta_c)} \tag{21}$$

Substituting (21) into $\sin\alpha_P = R_{prj}/r_P$, and from the (Cartesian) law of cosines,

$$\cot\alpha_P = \frac{\sqrt{1-A^2(1+e\cos(\theta'+\theta_c))^2}}{A(1+e\cos(\theta'+\theta_c))} \tag{22}$$

where $A = R_{prj}/a(1-e^2)$. Since $\theta'_c = 0$, (20) can be expressed as

$$R(\mathbf{r}_P) = \cos\theta' \cdot (u_T + h_Z \cdot \cot\alpha_{P_C}) + \sin\theta' \cdot v_T + N_{pm} \tag{23}$$

where $N_{pm} = \cos\theta'(h_Z \cot\alpha_P/\cos\theta' - h_Z \cot\alpha_{P_C})$ denotes distortion. Substitute (22) into N_{pm},

$$N_{pm} = \cos\theta' \cdot h_Z \cdot \left(\frac{\sqrt{1-A^2(1+e\cos(\theta'+\theta_c))^2}}{A(1+e\cos(\theta'+\theta_c))\cos\theta'} - \frac{\sqrt{1-A^2(1+e\cos\theta_c)^2}}{A(1+e\cos\theta_c)} \right) \tag{24}$$

From (23), (18) can be expressed as

$$S_Z(k', \mathbf{r}_P) = \exp\{-j(k_x \cdot (x_T + x_{T\text{off}}) + k_y \cdot (y_T + y_{T\text{off}})\} \cdot \exp\{-jk_P \cdot N_{pm}\} \tag{25}$$

where $x_{T\text{off}}$ and $y_{T\text{off}}$ denote the offsets along X and Y axes, respectively

$$\begin{aligned} x_{T\text{off}} &= h_Z \cdot \cot\alpha_{P_C} \cdot \cos\theta_c \\ y_{T\text{off}} &= h_Z \cdot \cot\alpha_{P_C} \cdot \sin\theta_c \end{aligned} \tag{26}$$

N_{pm} will cause scatterers defocused if $h_Z \geq h_{HOF}$. To guarantee image quality, it requires that the phase variation caused by third term on the right of (25) to be kept within $\pi/4$, i.e.,

$$|k_P N_{pm}| \leq \pi/4 \tag{27}$$

Let $R_{pm} = \left(\frac{\sqrt{1-A^2(1+e\cos(\theta'+\theta_c))^2}}{A(1+e\cos(\theta'+\theta_c))\cos\theta'} - \frac{\sqrt{1-A^2(1+e\cos\theta_c)^2}}{A(1+e\cos\theta_c)} \right)$, then from (27)

$$h_{HOF} = \frac{\pi}{4 \cdot |k_{u\max}| \cdot |\Delta R_{pm}|} \tag{28}$$

where $|k_u|_{\max} \approx k_{r\max} \cos\theta' \cdot \sin i \cdot (r_P/\rho_{0\text{mid}})$. It is worth to notice that different sub-apertures correspond to different values of R_{pm} and h_{HOF}.

3.2. Reconstruction Procedure and Computational Complexity

This subsection gives the practical implementation of the improved PFA. According to (28), the total target scene of spherical crown shape is divided into several sub-scenes with the altitude $h_n = H_{sph} - (2n - 1)h_{HOF}$, $n = 1, 2 \cdots N$, $N = \lceil H/2h_{HOF} \rceil$ (H is the height of the spherical crown) and breadth $D = 2h_{HOF}$ in Z direction as shown in Figure 6. The implementation procedure is summarized in Figure 7. Assume the number of range samples is N_r, the number of azimuth samples is N_a, the imaging size is $N_s \times N_s$, and the 1D interpolator length is M_{ker}.

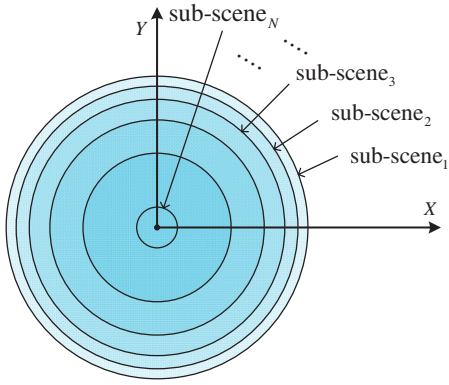

Figure 6. Sketch map of sub-scene mosaic.

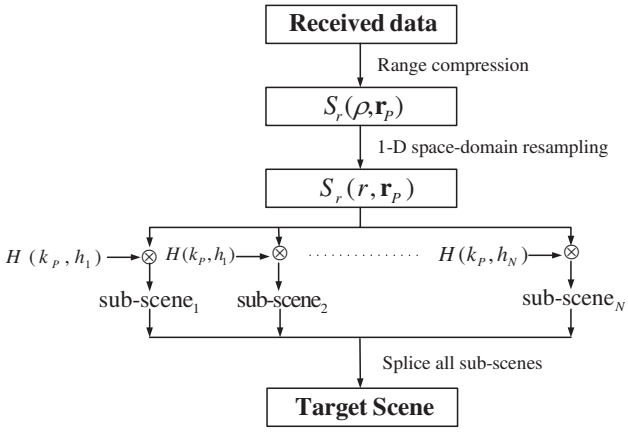

Figure 7. Flowchart of the improved PFA.

Step1: Map ρ to r via 1D resampling of the range compressed data $S_r(\rho, \mathbf{r}_P)$. The computational complexity is $O(M_{\text{ker}} N_a N_r)$.

Step2: 1D range FFT of $S_r(r, \mathbf{r}_P)$. The computational complexity is $O(N_a N_r \log N_r)$.

Step3: Multiply $S_r(k', \mathbf{r}_P)$ with a set of reference function $H(k_P, h_n)$ and obtain a set of $S_z^n(k', \mathbf{r}_P)$. The computational complexity is $O(N_a N_r N)$.

Step4: Convert every polar format data $S_z^n(k', \mathbf{r}_P)$ to Cartesian format data $S_Z(k_x, k_y)$ via a 2D interpolation. The computational complexity is $O(M_{\text{ker}}^2 N_s^2 N)$.

Step5: 2D IFFT of the output signal to obtain the 2D image of sub-scenes. The computational complexity of this step is $O(N_s^2 \log N_s)$.

Step6: Splice all the sub-scenes into a whole scene. The computational complexity of this step is $O(N_s^2)$.

The total computational complexity of the improved PFA is $O((M_{\text{ker}}^2 + \log N_s) N_s^2 N)$. The computational complexity of BP algorithm, which is based on pixel-by-pixel processing, is $O(\eta_{\text{ker}} N_a N^2 N)$. The improved PFA is apparently more efficient than BP.

3.3. Phase Error Analysis

In (12), when mapping ρ to r, all the scatterers were assumed locating on the surface of earth. In fact, the signal of targets with height $H_T \neq 0$ in frequency domain is

$$S_r(k', \mathbf{r}_P) = \exp\left\{-jk' \frac{r_P^2 + r_T^2 - R^2(\mathbf{r}_P, \mathbf{r}_T)}{2r_P}\right\} = \exp\{j\Phi_{Equ} + j\Phi_{err}\} \quad (29)$$

where

$$\begin{aligned} \Phi_{Equ} &= -k' \cdot r_{Equ} = -k' \left(r_P^2 + R_e^2 - R^2(\mathbf{r}_P, \mathbf{r}_T)\right) / (2r_P) \\ \Phi_{err} &= -k' \cdot (r - r_{Equ}) = -k' \left(R_e^2 - r_T^2\right) / (2r_P) \end{aligned} \quad (30)$$

From (30), Φ_{err} is proportional to $(r_T^2 - R_e^2)$, when $r_T = R_e$, $\Phi_{err} = 0$. That is to say, the targets located exactly on earth surface can be accurately reconstructed. Utilizing $\mathbf{r}_P$ from (8) and $\cos\nu/(\cos\theta_P \sin\alpha) = 1/\sin i$, it yields

$$\Phi_{err} = -k_P \cos\theta' \cdot \frac{(R_e^2 - r_T^2)}{2a(1-e^2)\sin\alpha_P \cos\theta'} - k_x \frac{e(R_e^2 - r_T^2)}{2a(1-e^2)\sin i} = \Phi_l + \Phi_h \quad (31)$$

where Φ_l is linear phase error, Φ_h is high frequency phase error. Then

$$\begin{aligned}\Phi_l &= -k_u \cdot \text{mean}\left(\frac{1}{\sin\alpha\cos\theta'}\right)\cdot\frac{(R_e^2-r_T^2)}{2a(1-e^2)} - k_x\frac{e(R_e^2-r_T^2)}{2a(1-e^2)\sin i}\\ &= -k_x\cdot x_{\text{off}} - k_y\cdot y_{\text{off}}\\ \Phi_h &= -k_u\cdot\left(\frac{1}{\sin\alpha\cos\theta'} - \text{mean}\left(\frac{1}{\sin\alpha\cos\theta'}\right)\right)\cdot\frac{(R_e^2-r_T^2)}{2a(1-e^2)}\end{aligned} \tag{32}$$

where x_{off} and y_{off} denote offsets of target position in X and Y axes caused by Φ_l which has no effect on the focusing quality.

$$\begin{aligned}x_{\text{off}} &= \cos\theta_c\cdot\text{mean}\left(\frac{1}{\sin\alpha\cos\theta'}\right)\cdot\frac{(R_e^2-r_T^2)}{2a(1-e^2)} + \frac{e(R_e^2-r_T^2)}{2a(1-e^2)\sin i}\\ y_{\text{off}} &= \sin\theta_c\cdot\text{mean}\left(\frac{1}{\sin\alpha\cos\theta'}\right)\cdot\frac{(R_e^2-r_T^2)}{2a(1-e^2)}\end{aligned} \tag{33}$$

From (33), the image distortion increases as the height of target increases. The high frequency phase error Φ_h might lead to defocusing for scatterers far away from the reference surface. To guarantee image quality, the variation of Φ_h needs to be kept within $\pi/4$, i.e.,

$$\left|k_{P_{\max}}\frac{(R_e^2-r_T^2)}{2a(1-e^2)}\Delta\mu(t_m)\right| \le \pi/4 \tag{34}$$

where $\mu(t_m) = \cos\theta'\cdot(\frac{1}{\sin\alpha\cos\theta'} - \text{mean}(\frac{1}{\sin\alpha\cos\theta'}))$. Thus the effective imaging size is

$$\left|R_e^2 - r_T^2\right| \le \frac{\pi a(1-e^2)}{2\left|\Delta\mu(t_m)\right|\cdot k_{r_{\max}}\sin i}\left(\frac{\rho_0}{r_P}\right)_{\text{mid}} \tag{35}$$

As long as the height of scatterer $H_T = r_T - R_e$ satisfies (35), it could be well focused.

3.4. Resolution Analysis

Let $\mathbf{r}_{ins}$ be the position vector of the point that is the intersection of perigee-apogee vector and Z axis, $\mathbf{r}_{ins} = (0,\ 0,\ a(1-e^2)\cos i)$ as shown in Figure 4. γ is the angle between the underside of the truncated cone and k_x-k_y plane, $\gamma = \arcsin(\mathbf{r}_T\sin\alpha_T/|\mathbf{r}_{ins}-\mathbf{r}_T|)$. Satellite-to-target vector is $\widetilde{\mathbf{r}}(t_m) = \mathbf{r}_P(t_m) - \mathbf{r}_T$, while center of sub-aperture corresponds to $\widetilde{\mathbf{r}}_c = \widetilde{\mathbf{r}}(\widetilde{\theta}_c)$. Let ϑ be spatial angle that sub-aperture has swept, then $\Delta\widetilde{\theta} = \widetilde{\mathbf{r}}(\widetilde{\theta}_c),\ \widetilde{\mathbf{r}}(\widetilde{\theta}_c+\vartheta/2)$, and $\eta = \widetilde{\mathbf{r}}(\widetilde{\theta}_c),\ \widetilde{\mathbf{r}}(\widetilde{\theta}_c+\pi)$ (see Figure 8). Rotate X-Y plane by $\widetilde{\theta}_c$ on Z axis, and define the rotated plane as $\widetilde{U}-\widetilde{V}$.

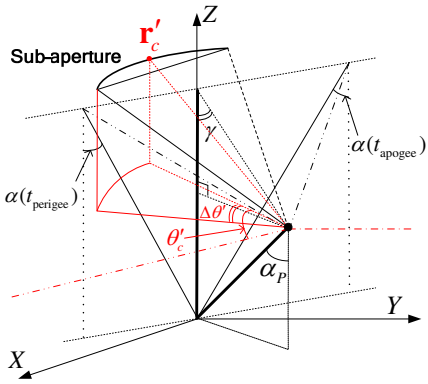

Figure 8. Spatial geometry of target.

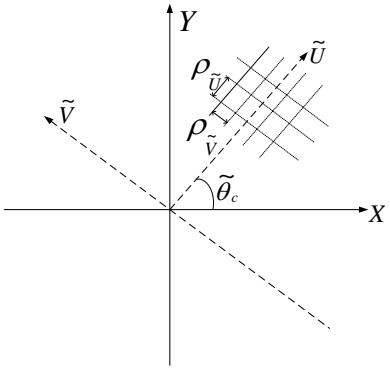

Figure 9. Image resolution.

$(k_x,\ k_y)$ are projected into $(k_{\widetilde{U}},\ k_{\widetilde{V}})$, then the bandwidth

$$\begin{aligned} B_{\widetilde{U}} &= k_{\max} \cdot \left| r'\left(\widetilde{\theta}_c + \Delta\widetilde{\theta}\right) - r'\left(\widetilde{\theta}_c - \Delta\widetilde{\theta}\right)\right| \cdot \cos\left(\frac{\eta}{2}\right) \cdot \sin\left(\Delta\widetilde{\theta}\right) \\ B_{\widetilde{V}} &= \left(k_{\max} - k_{\min} \cdot \cos\left(\Delta\widetilde{\theta}\right)\right) \cdot \cos\left(\frac{\eta}{2}\right) \cdot \cos(\gamma) \end{aligned} \tag{36}$$

Finally, the range resolution and the cross-range resolution are $\rho_{\widetilde{U}} = \pi/B_{\widetilde{U}}$, $\rho_{\widetilde{V}} = \pi/B_{\widetilde{V}}$, respectively, as shown in Figure 9.

4. NUMERICAL SIMULATION

In this section, the imaging focusing capabilities of the improved PFA in GeoCSAR configuration are investigated and verified by means of numerical simulations. A sub-scene (third sub-scene) in the whole scene is chosen for imaging as shown in Figure 10. Altitude of third sub-scene in Z axis is $h_3 = 6334.5\,\text{km}$ and breadth in Z axis is $h_{HOF} = 2.6\,\text{km}$. The targets are located on the top edge and bottom edge of the sub-scene. The distance spacing of targets on the ground is 500 m.

A $50\,\text{m} \times 5000\,\text{m}$ area in the sub-scene is chosen to display. The center of the area is $(83.1942°\text{N}, 0.1895°\text{E})$. The targets locate along the same latitude in the same area. Assuming that all the targets are located exactly on the earth surface, and the image quality of targets are the same in the coverage scene. For the given system parameters of Table 1, h_{HOF} calculated via (28) is $h_{HOF} = 1.3546\,\text{km}$ and the range of scatterer height calculated with (35) is $|H_T| \leq 9.11\,\text{km}$.

Table 1. Main system and processing parameters.

Parameters	Values
Orbit inclination i_0	0.1 rad
Orbit eccentricity e_0	0.05
Argument of perigee ω_0	$\pi/2$ rad
Carrier frequency f_c	1.3 GHz
Signal bandwidth B	150 MHz
Sampling rate f_s	250 MHz
Pulse Repetition Frequency	112 Hz

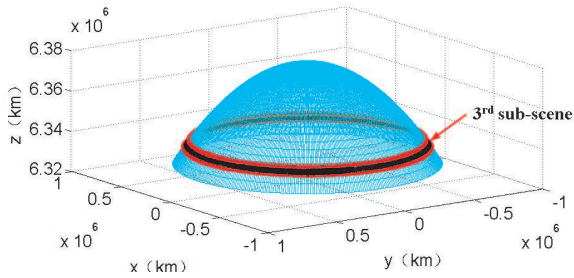

Figure 10. Sketch map of a sub-scene in whole imaging scene.

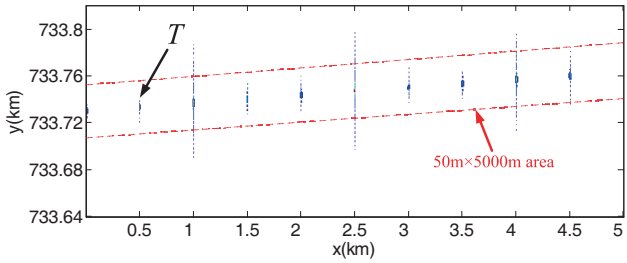

Figure 11. Imaging result of the chosen area, top edge of the third sub-scene.

Figure 11 shows imaging result of the chosen area. The plane that parallels X-Y plane with altitude h_3 in Z axis is chosen as focus plane. All targets are accurately reconstructed. From (26), there are linear offsets of target position along X and Y axis. After geometric correction, the focused targets are relocated at the correct position.

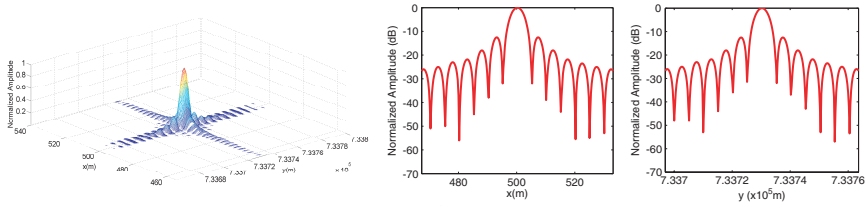

(a) Spread Function (b) Range profile (c) Azimuth profile

Figure 12. Imaging result of target T via BP algorithm.

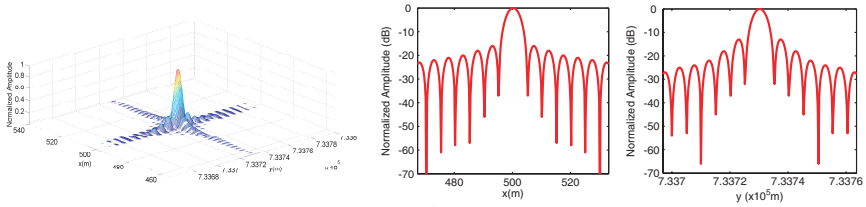

(a) Spread Function (b) Range profile (c) Azimuth profile

Figure 13. Imaging result of target T via improved PFA.

Table 2. Imaging quality comparison between BP algorithm and improved PFA.

Target T	BP algorithm			Improved PFA		
	Res. (m)	PSLR (dB)	ISLR (dB)	Res. (m)	PSLR (dB)	ISLR (dB)
Range	8.8947	−13.2732	−10.3321	8.9440	−13.2596	−9.9807
Azimuth	8.8960	−13.2853	−10.3554	8.9075	−13.2781	−10.0766

Since the targets distribute along the same latitude, the focused image of targets on the focus plane is an arc.

In order to show more details of the imaging results, spread function of target T (as shown in Figure 11) is shown in Figure 12(a). The azimuth and range profile are shown in Figure 12(b) and Figure 12(c). The same target T has also been imaged with BP algorithm for comparison, and corresponding imaging results are shown in Figure 13. Quality metric of imaging results from BP algorithm and the improved PFA are listed in Table 2, including 3 dB impulse response width (IRW), peak sidelobe ratio (PSLR) and integrated

sidelobe ratio (ISLR). From Table 2, it can be concluded that the improved PFA has a comparable performance to BP algorithm, but the improved PFA, as a frequency domain algorithm, deals with the echoed data simultaneously and works more efficiently than BP algorithm.

5. CONCLUSIONS

This paper has proposed an improved PFA imaging algorithm for GeoSAR which undergoes a near-circular track. Imaging geometry and corresponding imaging model with orbit perturbation considered has been derived, which helps to ensure accurate slant range between antenna and targets. By assuming spherical wavefronts instead of planar wavefronts, the proposed algorithm focuses GeoCSAR raw data on a spherical reference surface (ground surface). Thereby the size of focused scene is no longer limited by the range curvature phase error. The implementation procedure has been presented while the computational complexity are calculated, which shows the efficiency of the proposed algorithm. Phase error and achievable resolution have been analyzed, which assesses feasibility of the imaging algorithm. Numerical simulation has been performed and the results about the imaging quality further validate feasibility of the imaging algorithm and correctness of the analysis.

REFERENCES

1. Bruno, D., S. E. Hobbs, and G. Ottavianelli, "Geosynchronous synthetic aperture radar: Concept design, properties and possible applications," *Acta Astronaut*, Vol. 59, No. 1–5, 149–156, 2006.
2. Bruno, D. and S. E. Hobbs, "Radar imaging from geosynchronous orbit: Temporal decorrelation aspects," *IEEE Trans. Geosci. Remote Sens.*, Vol. 48, No. 7, 2924–2929, 2010.
3. Sun, J., S. Mao, G. Wang, and W. Hong, "Extended exact transfer function algorithm for bistatic SAR of translational invariant case," *Progress In Electromagnetics Research*, Vol. 99, 89–108, 2009.
4. Soop, E. M., *Handbook of Geostationary Orbits*, Springer, 1994.
5. Tan, W. X., W. Hong, Y.-P. Wang, and Y.-R. Wu, "A novel spherical-wave three-dimensional imaging algorithm for microwave cylindrical scanning geometries," *Progress In Electromagnetics Research*, Vol. 111, 43–70, 2011.

6. Soumekh, M., "Reconnaissance with slant plane circular SAR imaging," *IEEE Trans. Image Processing*, Vol. 5, No. 8, 1252–1265, 1996.
7. Lin, Y., W. Hong, W. X. Tan, and Y. R. Wu, "Extension of range migration algorithm to squint circular SAR imaging," *IEEE Geosci. Remote Sens. Lett.*, Vol. 8, No. 4, 651–655, 2011.
8. Carrara, W. G., R. S. Goodman, and R. M. Majewski, *Spotlight Synthetic Aperture Radar: Signal Processing Algorithms*, Artech House, Norwood, MA, 1995.
9. Mao, X. H., D.-Y. Zhu, L. Ding, and Z. D. Zhu, "Comparative study of RMA and PFA on their responses to moving target," *Progress In Electromagnetics Research*, Vol. 110, 103–124, 2010.
10. Sun, J. P., S. Y. Mao, G. H. Wang, and W. Hong, "Polar format algorithm for spotlight bistatic SAR with arbitrary geometry configuration," *Progress In Electromagnetics Research*, Vol. 103, 323–338, 2010.
11. Mao, X. H., D. Y. Zhu, and Z. D. Zhu, "Signatures of moving target in polar format spotlight SAR image," *Progress In Electromagnetics Research*, Vol. 92, 47–64, 2009.
12. Nie, X., D.-Y. Zhu, and Z. D. Zhu, "Application of synthetic bandwidth approach in SAR polar format algorithm using the deramp technique," *Progress In Electromagnetics Research*, Vol. 80, 447–460, 2008.
13. Wang, X., D.-Y. Zhu, and Z.-D. Zhu, "An implementation of bistatic PFA using chirp scaling," *Journal of Electromagnetic Waves and Applications*, Vol. 24, No. 5–6, 745–753, 2010.
14. Chen, C. W., "Modified polar format algorithm for processing spaceborne SAR data," *Proc. IEEE Radar Conference*, 44–49, 2004.